Abstract (250 Words)

The Scintillation Observations and Response of The Ionosphere to Electrodynamics (SORTIE) mission is a 6U CubeSat that has been making ionospheric measurements at 420 km altitude since February 19, 2020. The SORTIE sensor suite includes an Ion Velocity Meter (IVM), which is used in the present study to detect and characterize Traveling Ionospheric Disturbances (TIDs). On July 11, 2020 the SORTIE orbit passed over near-concentric TIDs that were seen in the Total Electron Content (TEC) data from ground-based Global Positioning System receivers distributed across the COntiguous United States (CONUS). The TID wave characteristics estimated from the IVM data agree well with those determined from the ground-based TEC data. The wave periods derived from the SORTIE data are shorter than the TID periods in the TEC data but are anticipated and explained in terms of the classical Doppler effect. A numerical simulation was performed using the Weather Research and Forecasting (WRF) model that shows excitation of atmospheric gravity waves (AGWs) from a deep convective storm over Texas preceding TID observations by SORTIE. We show that these AGWs were observed at stratospheric heights in close proximity to the convective storm by the Atmospheric Infrared Sounder onboard the NASA Aqua satellite, and in the lowermost mesosphere by the Cloud Imaging and Particle Size instrument onboard the NASA Aeronomy of Ice in the Mesosphere satellite. These storm-generated AGWs, or the associated higher-order AGWs, are the likely sources of the TIDs observed in the ground-based TEC and SORTIE IVM data.

Plain Language Summary (200 Words)

Scintillation Observations and Response of The Ionosphere to Electrodynamics (SORTIE) is a miniature satellite that measures variations in the Earth's ionosphere. SORTIE was deployed from the International Space Station on February 19, 2020 and is orbiting the Earth at 420 km altitude. In this study, we use SORTIE measurements from July 11, 2020 to study periodic ion density perturbations caused by Atmospheric Gravity Waves (AGWs). These types of perturbations are called Traveling Ionospheric Disturbances (TIDs). We compare the SORTIE measurements of TIDs to ionospheric Total Electron Content (TEC) data from ground-based Global Positioning System receivers in the United States. The two datasets show good agreement with regard to the wave characteristics of the TIDs. The TEC data show concentric rings of wave activity. Results from the Weather Research and Forecasting (WRF) model show a deep convection system over Texas that generated AGWs with a concentric ring pattern. A similar pattern was also seen in satellite measurements of the stratosphere and mesosphere. The results show that AGWs excited by deep convection in the lower atmosphere or the higher-order AGWs created by the primary AGWs are the likely sources of the observed TIDs in the TEC data and the SORTIE measurements.

Key Points:

1. We show the first observation of TIDs by SORTIE at 420 km altitude above a deep convection system over Texas.
2. Model simulation and corroborating satellite and ground-based data show that these TIDs are induced by vertically propagating gravity waves.
3. The TID periods in the SORTIE IVM data are Doppler shifted due to the satellite velocity relative to the wavefronts.

1. Introduction

The Scintillation Observations and Response of The Ionosphere to Electrodynamics (SORTIE) mission is a 6U CubeSat designed to study the global distribution of wave-like structures in the plasma density of the ionospheric F-region and determine their possible role in the growth of plasma instabilities. The SORTIE mission, funded by the NASA Heliophysics Division, was launched aboard the SpaceX CRS-19 Dragon mission to the International Space Station on December 5, 2019 (17:29:24 UT) and subsequently inserted into a near-circular orbit on February 19, 2020 at ~420 km altitude with ~51.6° inclination. The SORTIE sensor suite consists of a miniature Ion Velocity Meter (IVM) and a micro-Planar Langmuir Probe (PLP) [Crowley et al., 2016]. The IVM sensor provides the temperature, composition, and vector velocity of the ionospheric plasma. The PLP instrument on SORTIE is designed to provide high-resolution plasma density and temperature measurements.

The science goals of the SORTIE mission are:

1. To discover the sources of wave-like plasma perturbations in the F-region ionosphere.
2. To determine the relative role of dynamo action and more direct mechanical forcing in the formation of wave-like plasma perturbations.

The wave-like perturbations in the plasma density, which SORTIE is designed to study, occur over a range of scales, in both the spatial and temporal domains. In this paper, we focus on a class of wave-like disturbances, called Traveling Ionospheric Disturbances (TIDs), induced by atmospheric gravity waves (AGWs). This study presents the first measurements of TIDs in the ion density measurements from the IVM sensor on the SORTIE CubeSat.

The TID features presented in this study are wave-like perturbations in the ionosphere, generally considered to be signatures of AGWs propagating through the ionosphere. Hines [1960, 1967] provided a theoretical foundation explaining the occurrence of TIDs and their relationship to AGWs. More recent theoretical work describing this relationship was presented in Vadas & Nicolls [2009] and Nicolls et al. [2014]. However, various aspects of the TIDs, such as the seasonal dependence of their occurrences, correlation with any geophysical indices, morphology, and evolution of TIDs, etc., lack a comprehensive explanation. In recent years, Total Electron Content (TEC) data from distributed Global Positioning System (GPS) receiver networks in the CONtiguous United States

(CONUS) have been used to "image" these TIDs [Nishioka et al., 2013; Azeem et al., 2015; Azeem et al. 2017; Azeem and Barlage, 2017; Vadas and Azeem, 2021]. Since TEC is a line integrated quantity weighted by the maximum ionospheric density, these TIDs in GPS data are assumed to be representative of the underlying AGWs at the F2 peak altitude (between ~250 and ~300 km). In this study, we present the first measurements of TIDs in the SORTIE in-situ ion density data at 420 km altitude. We show that the TIDs seen in the SORTIE data share similar spectral and wave characteristics as those derived from the ground-based TEC data. We also show that these TIDs were centered above a deep convection system over Texas that was the source of concentric AGWs and that these waves were also seen in satellite measurements of the stratosphere and mesosphere regions.

1. Traveling Ionospheric Disturbances on July 11, 2020

Figure 1 shows a sequence of maps of TIDs in the GPS TEC data over the CONUS on July 11, 2020 between 00:32 and 02:15 UT. Similar maps were generated, but not shown here, for the entire day at a cadence of 30 s. These maps have a resolution of 0.1° in latitude and longitude. The detailed methodology for generating these TID maps can be found in Azeem et al. [2015] and Azeem & Barlage [2017]. The maps in Figure 1 reveal several partial, concentric rings located over the South Central and the Midwest regions of the United States. The estimated center of these concentric waves was located near 36.1° N, 96.7° W. The TID amplitudes are largest to the east of the center, where the TIDs propagate radially eastward. The TIDs to the west of the center are either very weak or not present, possibly due to the dissipative filtering of the background neutral winds (see Vadas & Azeem [2021] and references therein for an explanation of filtering by the background wind). Similar partial, concentric TIDs in GPS TEC data have been reported by Nishioka et al. [2013], Azeem et al. [2015, 2017], and Vadas & Azeem [2021] and were associated with convective storm activity in the lower atmosphere. We note here that the strongest TID activity lasted for over two hours between 00:30 UT and 02:40 UT on July 11, 2020.

Next, we examine the parameters of the concentric TIDs within the red circles in Figure 1. Using wavelet analysis of the GPS TEC data we obtain their spectrograms and estimate the periodicities and horizontal wavelengths of the TID wave packet. This wavelet spectrogram method was previously used by Azeem et al. [2017] to estimate the periods and horizontal wavelengths of the TIDs in the GPS TEC data. Figure 2a shows the normalized spectrogram of the TIDs as a function of longitude at 36.1° N latitude. The white line in the figure represents the theoretical curve for the ground-based wave period ($_{\mathrm{r}}$) in a windless isothermal background atmosphere as defined in Azeem [2021]. We choose $z = 90$ km and $_{\mathrm{B}} = 11.5$ min so that the white line agrees reasonably well with the peak power in the spectrogram. Here, z is the altitude difference between the assumed AGW point source and the observation location and $_{\mathrm{B}}$ is the buoyancy period. Since 36.1° N is the latitude of the estimated ring center,

this spectrogram represents TIDs that propagate zonally outward from the center. As noted earlier, the western portions of these TIDs are either very weak or absent in the maps, which is why the spectrogram in Figure 2a does not show any features with significant power westward of 96.7° W longitude. The periods of the eastward propagating concentric TIDs are seen to increase approximately linearly with longitude, with $_{r}$ 12−27 min. The linear dependence of the TID periods in the spectrogram with the radial distance (R) from the center is consistent with the theoretical estimates of the ground-based periods of the AGW ($_{r}$) and illustrates the consistency between the data and idealized point source theory. Figure 2b shows the wavelet spectrum of horizontal wavelengths as a function of longitude at 36.1° N. TIDs with horizontal wavelengths between 100 km and 200 km dominate the spectrum and appear eastward of 96.7° W longitude.

Figure 3 shows the stratospheric gravity wave activity derived from the Atmospheric Infrared Sounder (AIRS) instrument's 4.3 m CO_2 channel-integrated radiance product [Hoffmann et al., 2013] preceding the TID observations in the TEC data. The AIRS instrument on the NASA Aqua satellite orbits Earth from pole-to-pole, approximately fifteen times each day. The orbit of the Aqua satellite is polar sun-synchronous with a nominal altitude of 705 km and an orbital period of 98.8 minutes. AIRS views the same area on Earth twice per day; once during a descending pass which occurs at 01:30 LT and once during the ascending pass at 13:30 LT. In Figure 3, we show the AIRS gravity wave image on July 10, 2020 at 13:30 LT (18:30 UT) that was closest in time to the TID observations shown in Figure 1. The AIRS data reveals wave features that are located in the same region as the concentric TIDs seen in GPS TEC data. The proximity of the gravity waves in AIRS data and the concentric TIDs in GPS TEC data suggest that they are part of the same event that generated disturbances in the stratosphere and the ionosphere.

The suggestion that a chain of events originating in the lower atmosphere led to the TEC TIDs described above is further supported by evidence of AGWs in the lowermost mesosphere from the Cloud Imaging and Particle Size (CIPS) instrument [McClintock et al., 2009] on the NASA Aeronomy of Ice in the Mesosphere (AIM) satellite [Russell et al., 2009]. AIM is in a near-polar, sun-synchronous orbit with ~15 orbits per day. CIPS is a 4-camera, nadir imager that measures scattered radiation at a wavelength of 265 nm throughout the sunlit portion of each orbit. The CIPS field of view is ~1000 km × 2000 km, with the long dimension oriented along the orbit track during the period of interest for the current study. As described by Randall et al. [2017], AGWs are inferred from periodic perturbations in the Rayleigh-scattered solar radiance; i.e., the Rayleigh Albedo Anomaly (RAA) data. The RAA weighting function peaks at an altitude of 50-55 km, where temperature profiles from the NASA Microwave Limb Sounder (not shown) indicate was in the lowermost mesosphere at the times and locations of the analysis here. Figure 4 shows CIPS RAA data acquired over the CONUS on July 9-11, 2020. Red ovals highlight regions of wave signatures near the same geographic location as the AIRS features shown in

Figure 3, with particularly strong concentric patterns evident on July 10, 2020. The presence of wave-like perturbations in the CIPS RAA data is consistent with repeated and/or persistent vertical propagation of AGWs from convective events in the troposphere.

We also performed a simulation using the Weather Research and Forecasting (WRF) model of AGWs over the region of interest from July 10, 2020 18:00 UT through July 11, 2020 06:00 UT. This period for the simulation was chosen because it captures the conditions in the lower atmosphere a few hours prior to the SORTIE measurements of the TIDs. The WRF model is based on fully-compressible, non-hydrostatic Navier-Stokes equations with physics packages of radiation, microphysics, convection, boundary layer, and land-air interaction [Skamarock et al., 2019]. For this study, the WRF model was specifically configured to simulate convectively generated gravity waves below 32 km. As illustrated in Figure 5, we used two nested domains, with grid spacings of 6 km and 2 km for the outer and interior domains, respectively. The interior 2-km domain covered most of the Great Plains from Nebraska to Texas. The terrain-following hybrid sigma-pressure vertical coordinate was used with its top at 5 hPa (~37 km) and 134 levels. The top 5 km serves as a damping layer to eliminate wave reflection from the upper boundary of the model. The 6-km domain was initialized with NCEP (National Center for Environmental Prediction) GDAS (Global Data Assimilation System) analysis on July 10, 2020 at 12:00 UT, and its lateral boundary was updated with a three-hourly GDAS analysis in terms of pressure, wind, temperature, moisture, and geopotential. The interior domain was activated 6 hours later at 18:00 UT using the 6-km domain forecast to allow the model to spin up and the mesoscale system to develop within the model domain. Cumulus convective processes were parameterized in the 6-km domain but explicitly resolved with parameterized microphysics in the 2-km domain. The GOES infrared imagery (not presented here) shows the development of a mesoscale convective system (MCS) in this region on the afternoon of July 10, 2020. It originated in the south of Amarillo, Texas and moved eastward to Oklahoma and started to decay in the late afternoon/early evening. The model simulation reveals excited gravity waves, which propagated vertically into the stratosphere. Figure 6 shows a snapshot of the simulated vertical velocity (w) and horizontal wind vector at 22:30 UT on July 10, 2020 at 30 km altitude. The AGW signatures are clearly exhibited in the patterns of the vertical velocity. Partial, concentric rings of AGWs are evident near 34-35° N, 101° W. The estimated ring center is located at 34.1° N, 101.8° W. The vertically propagating AGWs move to the east following the MCS in the simulation. Figure 7 is the altitudinal cross-section of the vertical velocity and air temperature through the MCS (from about 33° N, 102° W to 37° N, 100° W) at 22:30 UT on July 10, 2020. The vertical velocity is in the range of -7.1 m/s to +12.2 m/s. The deep convection near 34.1° N, 101.8° W penetrates to ~15 km, with the updraft up to 12.2 m/s. This deep convection generated an outward and upward propagating wave train that is reflected in both the air temperature and vertical velocity above 16 km. The excited AGWs are expected to continu-

ously propagate beyond the WRF model top to higher altitudes. The pattern of the simulated response is similar to the observed response seen in the TEC data: partial, concentric, outward-propagating rings. Note that the center of the rings in the WRF model simulation (at 34.1° N. 101.8° W) is 515.1 km from the center of the rings in the TEC at 36.1° N, 96.7° W. This offset distance can be explained as either due to the changing intervening horizontal wind (if the TIDs in the TEC are created by the primary AGWs) or by the offset location of the local body forces (i.e., horizontal accelerations) created by the dissipation of these convectively-generated AGWs [Vadas & Azeem, 2021].

1. **Results**

The near-circular orbit of SORTIE has an orbital period of 93.9 min, completing approximately 15.5 orbits per day. On July 11, 2020 a SORTIE orbit serendipitously sampled the region above the TIDs seen in GPS TEC data. In Figure 8, we overlay the SORTIE IVM measurement track on the TID activity seen in the GPS TEC data. We note here that the TID detection altitude is near 250 km (the altitude of maximum ionospheric density) whereas the SORTIE measurements are taken near 420 km altitude. The SORTIE pass shown in Figure 8 covers the UT range 04:29-04:43.

Quasi-periodic oscillations are seen in the 4-s sampled IVM ion density measurements during the interval when SORTIE passed through the region above the concentric TIDs. To quantify the characteristics of these wave-like perturbations in the SORTIE data, we first detrend it using a 3rd order polynomial fit and then compute the corresponding period and horizontal wavelength spectrograms. Figure 9a shows the IVM data (black line) during the SORTIE orbit segment in Figure 8 along with the fit (red line). The detrended IVM measurements during this interval are shown in Figure 9b. Quasi-periodic variations are evident in the detrended IVM data. Before we discuss the spectrograms, it is worth noting here that the TIDs in SORTIE IVM data will be Doppler shifted as the satellite moves toward or away from the wavefronts. The magnitude of the Doppler shift is a function of the angle ( ) at which the SORTIE satellite travels relative to the direction normal to the TID phase-fronts. It is easy to see that the observed Doppler shift is maximum when = 0° (satellite is moving directly towards the TIDs) or = 180° (satellite is moving directly away from the TIDs) while no Doppler shift is noted when = 90° (where satellite relative velocity normal to the TID phase front is zero). The Doppler-shifted TID periods exhibit a cyclical variation due to the relative motion of SORTIE and the TID phase fronts. Further details of the expected Doppler shift in the SORTIE data are presented in Appendix A. For illustrative purposes, in Figure 10, we show the expected Doppler shifts for TIDs with different periods and an assumed constant horizontal phase speed of c_H = 100 m/. We also assume that the TID source is stationary, which is reasonable as the SORTIE satellite velocity (V_{sat} = 7.6 km/s) is much faster than the sound speed in the thermosphere, and is, therefore, faster than any of these TIDs. We note that as the satellite moves away from the TID source with a relative velocity that is greater than c_H,

the Doppler shift leads to negative frequency values. However, as the wavelet spectrograms are computed for positive frequencies only (note: Parseval energy relation holds for wavelet transforms), we calculate and show the magnitudes of the Doppler-shifted periods in Figure 10. The inset in the figure shows a close-up view of the Doppler-shifted periods so that the different curves near $= 90°$ can be more easily differentiated from each other. The angular variations of the Doppler shift are such that the observed TID periods in the SORTIE data are mostly blue-shifted except for a small angular range, where $0 < v_{\mathrm{sat}}^{'} < c_H$, when the observed periods are redshifted. Here, $v_{\mathrm{sat}}^{'}$ is the projection of the satellite velocity vector along the direction of propagation of the TIDs (i.e., the direction perpendicular to the TID phase fronts). The figure (see inset) shows that at $= 90°$, the observed periods are equal to the TID periods. More details of the explanation of the Doppler shift in the SORTIE IVM data are provided in the appendix.

Next, we calculate the wavelet spectrogram of the SORTIE IVM data and compare it with the expected behavior predicted by Figure 10. Figure 11 shows the wavelet spectra of the observed TID periods and horizontal wavelengths seen in the IVM detrended data. Vadas & Azeem [2021] points out that for AGWs excited by a point source, the wave period and horizontal wavelength increase with the radial distance from the center. Therefore, in the context of the SORTIE observations presented here, longer period TIDs, which are at the outer edge of the near-concentric rings, will be sampled first, and then, as the satellite continues to travel, progressively shorter wave periods will be seen in the data. As SORTIE moves beyond the point of zero Doppler shift (defined here as the location where its velocity vector is perpendicular to the wave normal of the TIDs), the opposite behavior is seen. Progressively longer period waves are seen in the measurements as the satellite moves away from the TID pattern. It follows that as the SORTIE CubeSat approaches the outer rings of the TIDs, it will observe longer period waves first, which will undergo a large Doppler shift due to being small. As SORTIE continues to travel along its orbit, both the period of waves being observed and increase (decreasing Doppler shift). The resultant effect is that the observed periods in the spectrogram increase as a function of time. Near 4:36 UT, the SORTIE CubeSat is traveling perpendicular to the wave-normal of the TIDs, making the Doppler shift zero. After ~4:36 UT, as the SORTIE CubeSat moves away from the concentric rings (increasing), the observed period in the spectrogram decreases with time as the wave periods undergo progressively increasing Doppler shifts. Thus, the predicted pattern of the Doppler shift as a function of in Figure 10 does a reasonable job of explaining the shape of the SORTIE spectrogram in Figure 11a. Next, we analyze the perturbations in the IVM data to calculate the horizontal wavelength of the TIDs. Here, we note that because $v_{\mathrm{sat}} \gg c_{\mathrm{H}}$, SORTIE will see TIDs as if they were frozen in space. Figure 11b shows the spectrum of the along-track wavelength in the IVM data. The range of along-track wavelengths seen in the SORTIE data is in good agreement with the results of the TEC data (see Figure 2b). Again, SORTIE will first encounter the largest wavelengths on

the outer edges of the concentric ring pattern, followed by progressively decreasing wavelengths as it approaches the center. Once SORTIE passes the point of its closest approach to the center of the TID pattern, it will observe TIDs with along-track wavelengths that increase with the distance squared from the center of the concentric rings.

1. Summary and Conclusions

The SORTIE CubeSat has been operational since February 19, 2020, making in situ ionospheric plasma measurements at ~420 km altitude. In this paper, we present the first measurements of a TID event in the SORTIE IVM ion density data. On July 11, 2020 the SORTIE orbit passed through a region that was located above a set of concentric TIDs seen in ground-based GPS TEC over the CONUS. These concentric TIDs were centered over the U.S. South Central region and extended to the Midwest region. These concentric waves are shown to be centered over Oklahoma at 36.1° N and 96.7° W. The WRF simulation shows a deep convection event over this region spawning AGWs preceding the appearance of TIDs in the TEC data. The analysis of the TEC data shows that the period of the TIDs ranged from 12 to 27 min and their horizontal wavelengths were between 100 km and 250 km. Preceding the appearance of these TIDs in the TEC data, gravity wave activity was also seen in the AIRS and CIPS observations of the stratosphere and lower mesosphere, respectively, in the same region as the TIDs. The analysis of SORTIE IVM data shows wave-like perturbations with similar periods and horizontal wavelengths. The timing and regional proximity of the TIDs and AGWs on July 11, 2020 suggest that they all are associated with a common source in the lower atmosphere, which we posit is the deep convection, based on the WRF simulation. While the horizontal phase velocities of the observed TIDs (130-170 m/s) are not fast enough to rule out the presence of primary AGWs, the ring structure in the TEC data is suggestive of secondary AGWs. We also note that the concentric TIDs in the ground-based TEC data were azimuthally asymmetric. The AGWs in the stratosphere and mesosphere were observed to be propagating azimuthally north-northeast, east, and south-southeast because the prevailing middle atmosphere winds are westward. In contrast, the prevailing neutral winds in the thermosphere during this period were predominantly east-southeast. If the AGWs underlying the TIDs were primary waves, we would expect that the TIDs would instead have been propagating northwestward, because those AGWs propagating against the wind would have had increased vertical wavelengths and intrinsic horizontal phase speeds which would have enabled them to propagate higher into the thermosphere before dissipating from molecular viscosity [Vadas, 2007]. Instead, the TEC maps do not show the presence of northwestward traveling TIDs, thereby suggesting that the antisymmetric distribution of AGWs observed in the TEC data is likely due to the secondary AGWs created from the local horizontal body force (i.e., horizontal acceleration) created from the dissipation of primary AGWs from deep convection (similar to Vadas & Azeem, 2021). The reason for this is that these thermospheric body forces are typically created at z~180-200 km [Vadas & Crowley, 2010; Vadas & Liu, 2013]. Since the wind in the ther-

mosphere does not vary very much above this altitude, the secondary AGWs excited from these body forces are in the intrinsic reference frame of the background wind, and therefore will not be substantially filtered by the wind at higher heights. Thus, much of the antisymmetric secondary AGW pattern will be preserved in the TEC. Note that the secondary AGWs radiate away from a local zonal body force region in four directions; westward & upward, westward & downward, eastward & upward, and eastward & downward; the asymmetry occurs because no secondary AGWs radiate perpendicular to the force direction [Vadas et al., 2003]. The results presented here also highlight that the wave period computed using the SORTIE data will be Doppler shifted due to its motion relative to the TID wavefronts. TID maps, like those shown in Figures 1 and 7, can assist in the interpretation of the wave-like perturbations in the SORTIE IVM data.

This study provides strong evidence for the extent to which AGWs can propagate vertically and perturb the ionosphere. This study also demonstrates the ability of the SORTIE IVM instrument to measure TIDs. We note here that both the Ionospheric Connection Explorer (ICON) satellite [Immel et al., 2018] and Constellation Observing System for Meteorology, Ionosphere and Climate-2 (COSMIC-2) mission [Schreiner et al., 2020] carry similar IVM instruments. Based on the results presented in this paper, one can surmise that the SORTIE, ICON, and COSMIC-2 missions represent a unique opportunity for studying atmosphere-ionosphere interactions. TID measurements derived from IVM instruments on SORTIE, ICON, and COSMIC-2 at different altitudes, as well as measurements of stratospheric and mesospheric AGWs by instruments such as AIRS and CIPS, will complement each other and can provide an improved understanding of the vertical propagation of AGWs from the lower atmosphere through the ionosphere.

Appendix

Acknowledgments:

The SORTIE CubeSat and this work are supported by the NASA HQ grant 80NSSC18K0094 to Atmospheric & Space Technology Research Associates (ASTRA) LLC. IA also acknowledges support from NSF grant AGS-1552310. SLV was supported by NSF Grant AGS-1552315. The SORTIE IVM Level 2 ion density and GPS TEC data used in this study along with the WRF simulation results can be accessed on Zenodo (doi: 10.5281/zenodo.5083378). We acknowledge the use of publicly available ground-based GPS TEC data from the following data servers:

http://garner.ucsd.edu/, ftp://data-out.unavco.org/, ftp://geoid.hartrao.ac.za/, ftp://wcda.pgc.nrcan.gc.ca/. ftp://www.ngs.noaa.gov/ , ftp://ftp.ga.gov.au/, ftp://geoftp.ibge.gov.br/ , ftp://chain.physics.unb.ca/, ftp://cddis.gsfc.nasa.gov/.

AIRS data used in this study are available from the following website:

https://datapub.fz-juelich.de/slcs/airs/gravity_waves/index.html. AIM CIPS data are available at http://lasp.colorado.edu/aim/index.php and https://spdf.gsfc.nasa.gov/pub/data/aim/cips/data/RAA/. AIM is funded by the NASA Small Explorer program; CIPS data analysis for this paper was funded by NASA DRIVE grant 80NSSC20K0628 and Heliophysics Guest Investigator grant 80NSSC18K0775.

Appendix A

As the SORTIE satellite passes in close proximity to the concentric TIDs, the observed periods in the IVM data will exhibit varying levels of Doppler shifts due to the changing velocity of the satellite relative to the TID phase fronts. Figure A1 shows the SORTIE viewing geometry as it travels past the concentric TIDs. The observed frequency of the TIDs in the SORTIE IVM data is given by:

$$\nu = \nu_o \left(\frac{v + v'_{\mathrm{sat}}}{v} \right) \quad \text{(A1)}$$

where is the observed frequency, ν_o is the frequency of the TIDs, v is taken as the horizontal phase speed of the TID, and v'_{sat} is the projection of the satellite velocity vector normal to the TID phase front.

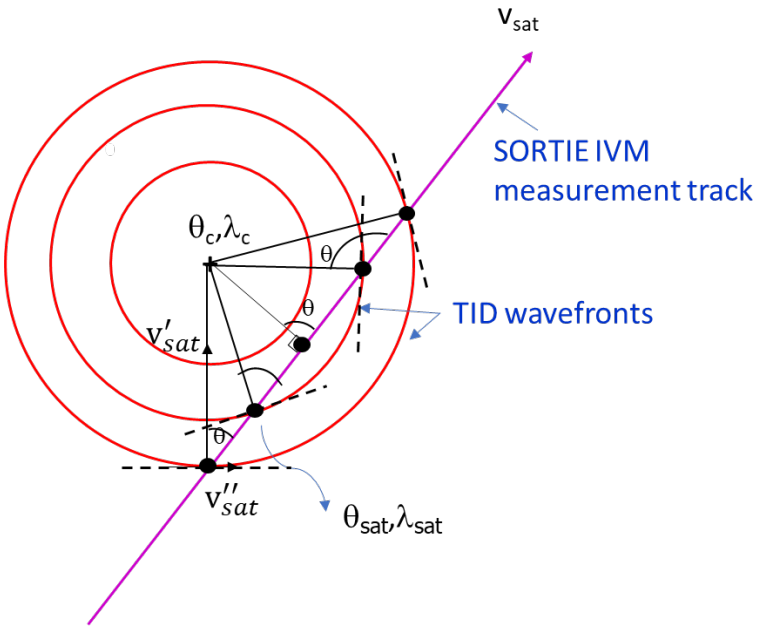

Figure A1. Schematic of the SORTIE viewing geometry of concentric TIDs. ($_c$, $_c$) and ($_{sat}$, $_{sat}$) are the co

The angular dependence of v'_{sat} is shown in Figure A2. As expected from Figure

A1, $v'_{sat} = v_{sat}$ for $= 0°$ and $= 180°$. The negative values in Figure A5 represent the satellite moving away from the concentric TIDs. At $= 90°$, the satellite velocity vector is entirely parallel to the TID phase front ($v''_{sat} = v_{sat}$) and $v'_{sat} = 0$. Therefore, at $= 90°$ when the satellite is moving tangentially to the TID phase fronts the Doppler shift is zero and the observed period is equal to the period of the TID.

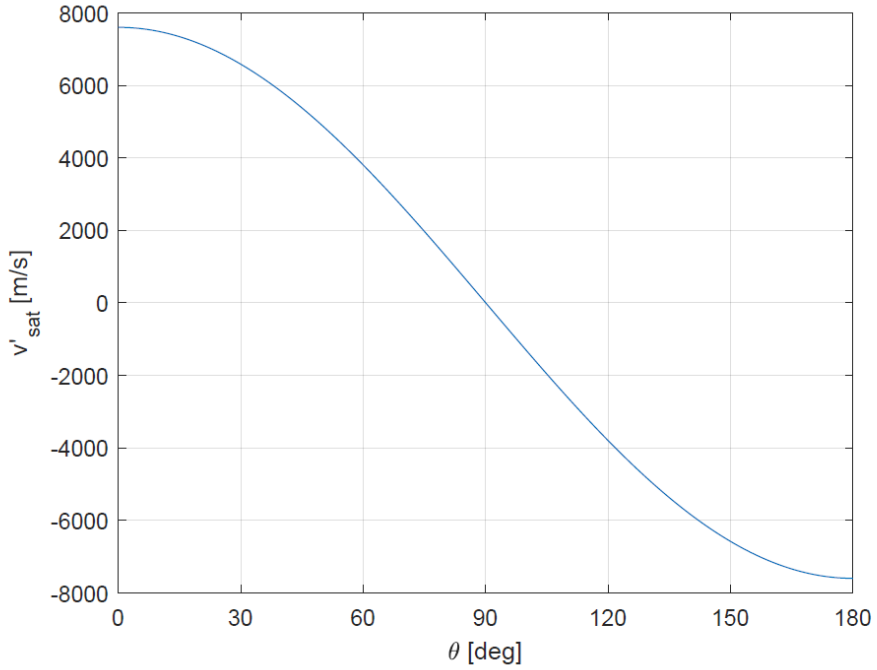

FigureA2. Angular variation of the component of the SORTIE satellite velocity (v_{sat}) perpendicular to the

Now, we calculate the Doppler-shifted period of a 10-min TID using the SORTIE observation geometry illustrated in Figure A1. We also assume that the horizontal phase speed of this TID (v) is 100 m/s. Figure A3a shows the variation in the Doppler-shifted frequency of the observed TID as a function of the angle . At $= 90°$, the period observed in the SORTIE data is the same as the TID period ($1/(10\times60) = 0.0017$ s^{-1}). The red square in Figure A3a marks the observed frequency at $= 90°$. The magnitude of the Doppler shift is shown in Figure A3b. The red dashed line in Figure A3b represents the TID period of 10 minutes. For the majority of the SORTIE pass over the concentric TID, the Doppler frequency is higher than the TID frequency (it is blue-shifted). However, over a small angular range, when $0 < v'_{sat} < c_H$, the Doppler-shifted frequency lies below the red dashed line (it is red-shifted). This angular de-

pendence of the Doppler frequency is reflected in Figure 10 which shows the magnitude of the Doppler-shifted TID periods in the SORTIE data for different wave periods ( ).

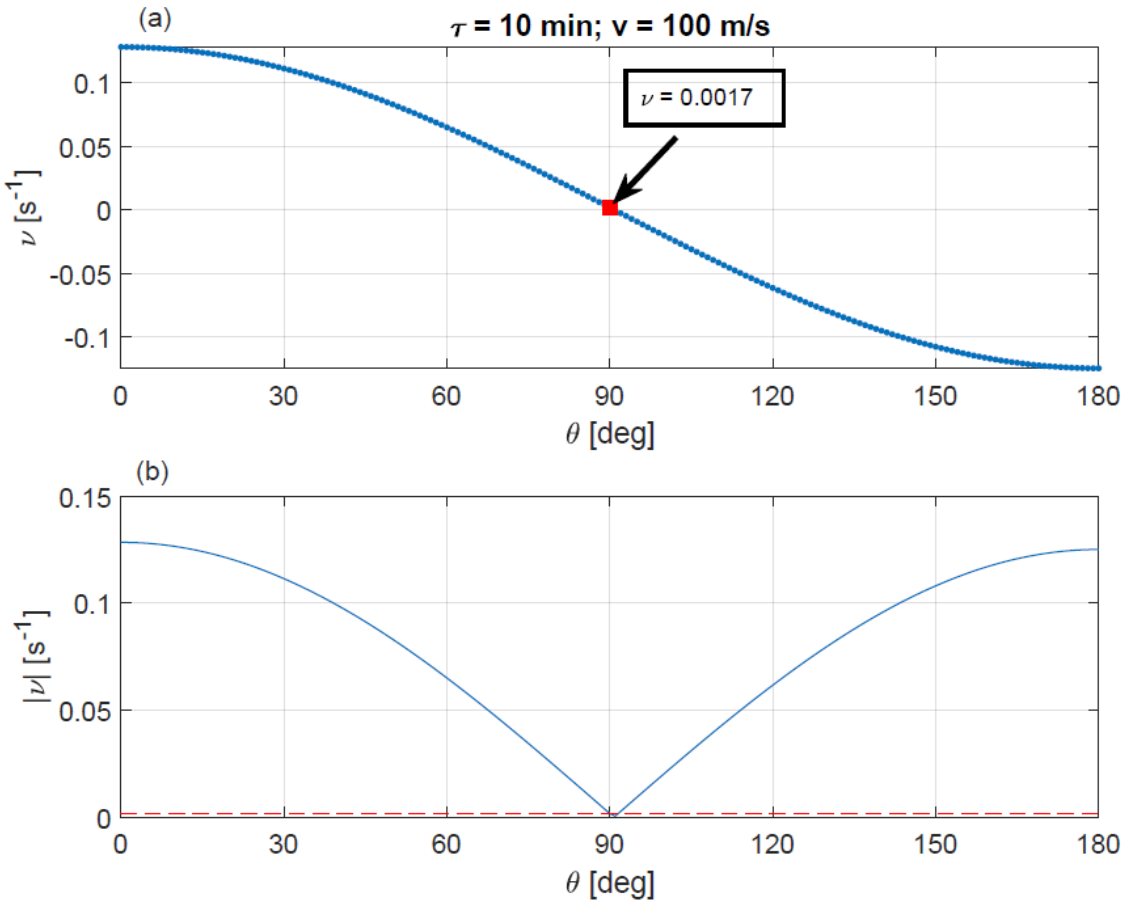

Figure A3. (a) Doppler-shifted frequency of a TID wave of a 10 min period and horizontal phase velocity of

Reference:

Azeem I (2021) Spectral Asymmetry of Near-Concentric Traveling Ionospheric Disturbances Due to Doppler-Shifted Atmospheric Gravity Waves, Front. Astron. Space Sci. 8:690480. doi: 10.3389/fspas.2021.690480

Azeem, I. & Barlage, M. (2017) Atmosphere-Ionosphere Coupling from Convectively Generated Gravity Waves, *Adv. Space Res.*, https://doi.org/10.106/j.asr .2017.09.029.

Azeem, I., S. L. Vadas, G. Crowley, and J. J. Makela (2017), Traveling ionospheric disturbances over the United States induced by gravity waves from the 2011 Tohoku tsunami and comparison with gravity wave dissipative theory, *J. Geophys. Res.: Space Physics*, 122, doi:10.1002/2016JA023659.

Azeem, I., J. Yue, L. Hoffmann, S. D. Miller, W. C. Straka III, and G. Crowley (2015), Multi-sensor profiling of a concentric gravity wave event propagating from the troposphere to the ionosphere, *Geophys. Res. Lett.*, 42, doi:10.1002/2015GL065903.

Crowley, G., C. Fish, M. Pilinski, E. Stromberg et al. (2016), Scintillation Observations and Response of The Ionosphere to Electrodynamics (SORTIE), Proceedings of the 30th Annual AIAA/USU SmallSat Conference, paper: SSC16-VI-3.

Drob, D. P., J. T. Emmert, J. W. Meriwether, J. J. Makela, E. Doornbos, M. Conde, G. Hernandez, J. Noto, K. A. Zawdie, S. E. McDonald, and et al. (2015), An update to the horizontal wind model (HWM): The quiet time thermosphere, *Earth and Space Science*, 2, 301–319, doi:10.1002/2014EA000089.

Hines, C. O. (1960), Internal atmospheric gravity waves at ionospheric heights, *Can. J. Phys.*, 38, 1441.

Hines, C.O. (1967), On the nature of travelling ionospheric disturbances launched by low-altitude nuclear explosions, *J. Geophys. Res.*, **72**, 1877-1882.

Hoffmann, L., X. Xue, and M. J. Alexander (2013), A global view of stratospheric gravity wave hotspots located with Atmospheric Infrared Sounder observations, *J. Geophys. Res.: Atmos.*, 118, 416-434, doi:10.1029/2012JD018658.

Immel, T. J., England, S. L., Mende, S. B. et al, (2018), The Ionospheric Connection Explorer Mission: Mission Goals and Design, *Sp. Sci. Rev.* 214, 13, doi:10.1007/s11214-017-0449-2.

McClintock, W. E., D. W. Rusch, G. E. Thomas, A. W. Merkel, M. R. Lankton, V. A. Drake, S. M. Bailey, and J. M. Russell III (2009), The cloud imaging and particle size experiment on the aeronomy of ice in the mesosphere mission: Instrument concept, design, calibration, and on-orbit performance, *J. Atmos. Sol. Terr. Phys.*, 71, 340–355.

Nicolls, M.J., S.L. Vadas, N. Aponte, and M.P. Sulzer (2014), Horizontal parameters of daytime thermospheric gravity waves and E region neutral winds over Puerto Rico, J. Geophys. Res. Space Physics, 119, doi:10.1002/2013JA018988.

Nishioka, M., T. Tsugawa, M. Kubota, *and* M. Ishii *(*2013*),* Concentric waves and short-period oscillations observed in the ionosphere after the 2013 Moore EF5 tornado*, Geophys. Res. Lett.,* 40*,* 5581–5586*, doi:*10.1002/2013GL057963.

Randall, C. E., et al. (2017), New AIM/CIPS global observations of gravity waves near 50–55 km, *Geophys. Res. Lett.*, 44, 7044–7052, doi:10.1002/2017GL073943.

Russell, J. M., III et al. (2009), Aeronomy of Ice in the Mesosphere (AIM): Overview and early science results, *J. Atmos. Sol. Terr. Phys.*, 71, 289–299, doi:10.1016/j.jastp.2008.08.011.

Schreiner, W. S., Weiss, J. P., Anthes, R. A., Braun, J., Chu, V., Fong, J., et al. (2020). COSMIC-2 radio occultation constellation: First results. *Geophysical Research Letters*, 47, e2019GL086841. https://doi.org/10.1029/2019GL086841.

Skamarock, W. C., Klemp, J. B., Dudhia, J., Gill, D. O., Liu, Z., Berner, J., Huang, X. (2019). A Description of the Advanced Research WRF Model Version 4 (No. NCAR/TN-556+STR). doi:10.5065/1dfh-6p97.

Vadas, S. L. & Azeem, I. (2021). Concentric secondary gravity waves in the thermosphere and ionosphere over the continental United States on March 25–26, 2015 from deep convection, *J. Geophys. Res.: Space Physics, 126,* e2020JA028275, https://doi.org/10.1029/2020JA028275.

Vadas, S. L., & G. Crowley (2010), Sources of the traveling ionospheric disturbances observed by the ionospheric TIDDBIT sounder near Wallops Island on 30 October 2007, J. Geophys. Res., 115, A07324, doi:10.1029/2009JA015053.

Vadas, S. L., Fritts, D. C., & Alexander, M. J. (2003). Mechanism for the generation of secondary waves in wave breaking regions. Journal of the Atmospheric Sciences, 60(1), 194– 214. https://doi.org/10.1175/1520-0469(2003)060<0194:MFTGOS>2.0.CO;2.

Vadas, S. L., and Liu, H.-L. (2013), Numerical modeling of the large-scale neutral and plasma responses to the body forces created by the dissipation of gravity waves from 6 h of deep convection in Brazil, J. Geophys. Res. Space Physics, 118, 2593– 2617, doi:10.1002/jgra.50249.

Vadas, S. L. & M. Nicolls (2009), Temporal evolution of neutral, thermospheric winds and plasma response using PFISR measurements of gravity waves, JASTP, 71, 740-770.

Vadas, S. L. and M. J. Nicolls (2012), The phases and amplitudes of gravity waves propagating and dissipating in the thermosphere: Theory, J. Geophys. Res, 117, A05322, doi:10.1029/2011JA017426.

Figures

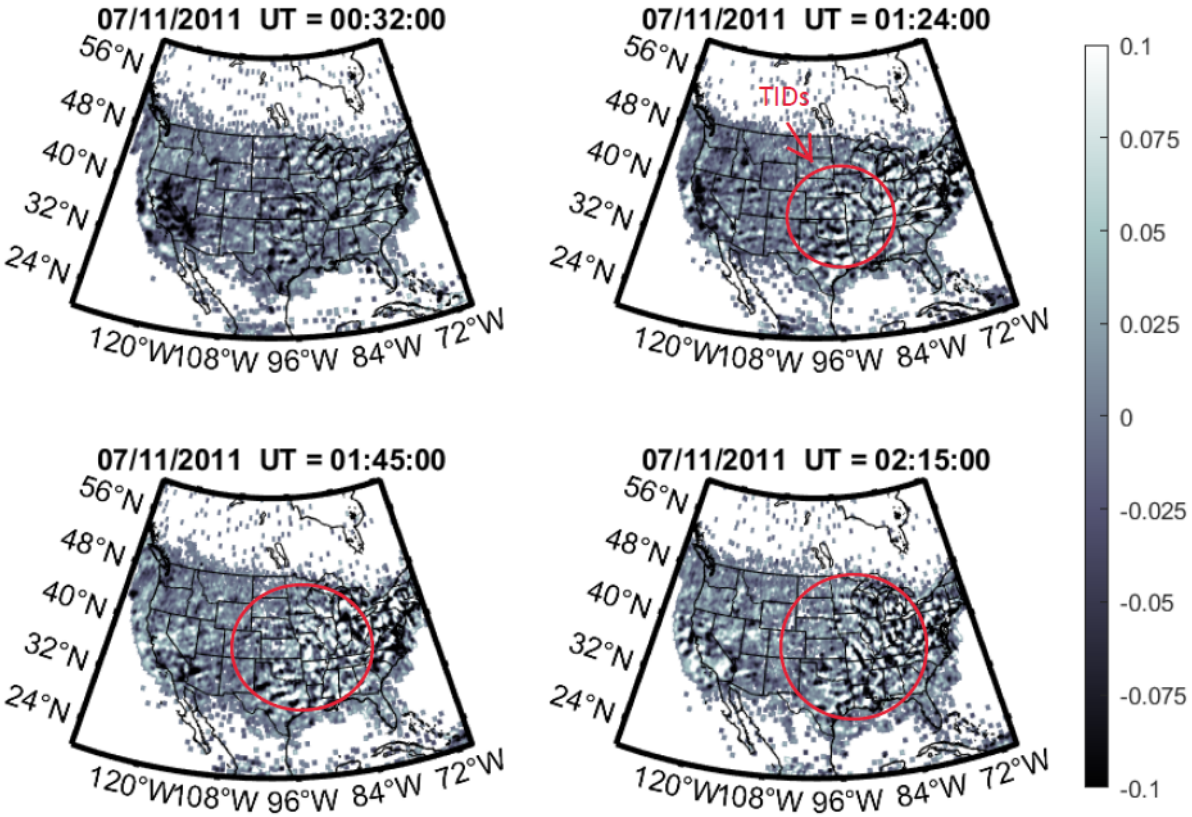

Figure 1. TEC perturbations over the CONUS in GPS TEC data at 00:32 UT, 01:24 UT, 01:45 UT and 02:15:00 UT on July 11, 2020. The red circles identify the concentric TID structures that are the subject of this study. The largest TIDs were seen in the TEC data between 00:30 UT and 02:30 UT. The color scale shows the TEC range in units of TECU (1 TECU = 10^{16} el/m^2).

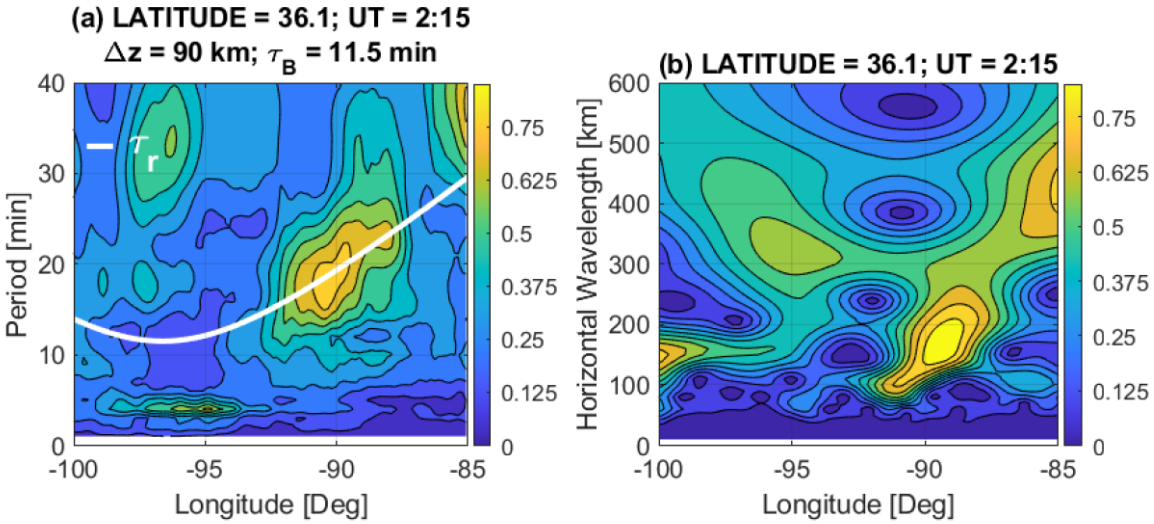

Figure 2. Wavelet spectrograms of the TEC perturbations at 36.1° N latitude. Results are shown for 02:15 UT on July 11, 2020 for the TIDs shown in Figure 1d. a) Spectrogram of TID as a function of longitude. The white curve shows the observed period of AGWs excited by a point source assuming z = 90 km, and $_B$ = 11.5 min in a windless and isothermal background atmosphere. b) Spectrum of TID horizontal wavelengths as a function of longitude for the same time and location as in (a).

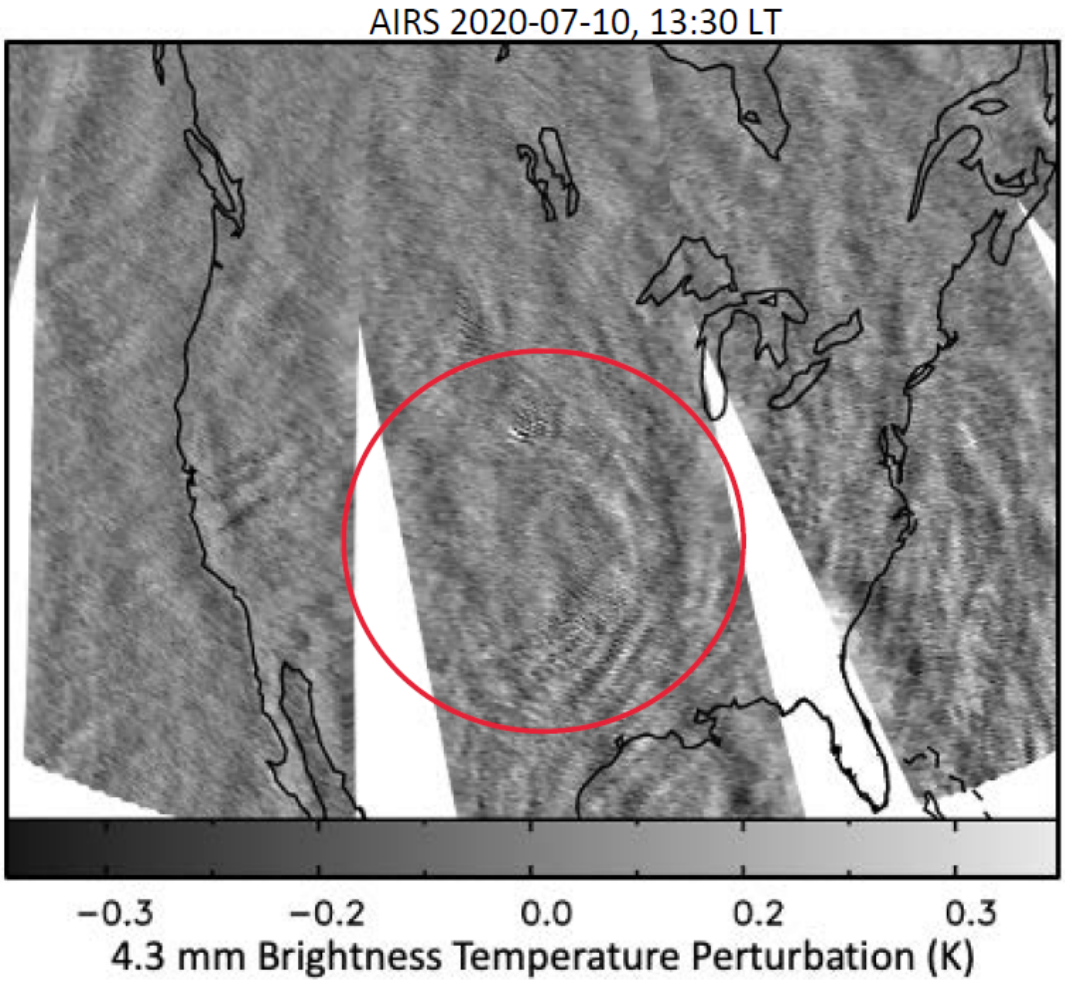

Figure 3. AIRS/Aqua observations of gravity waves preceding the TIDs seen in GPS TEC data. The red circle bounds the wave features that are located in the same region of CONUS as the concentric TIDs. This was the closest AIRS data in time to the TIDs shown in Figure 1.

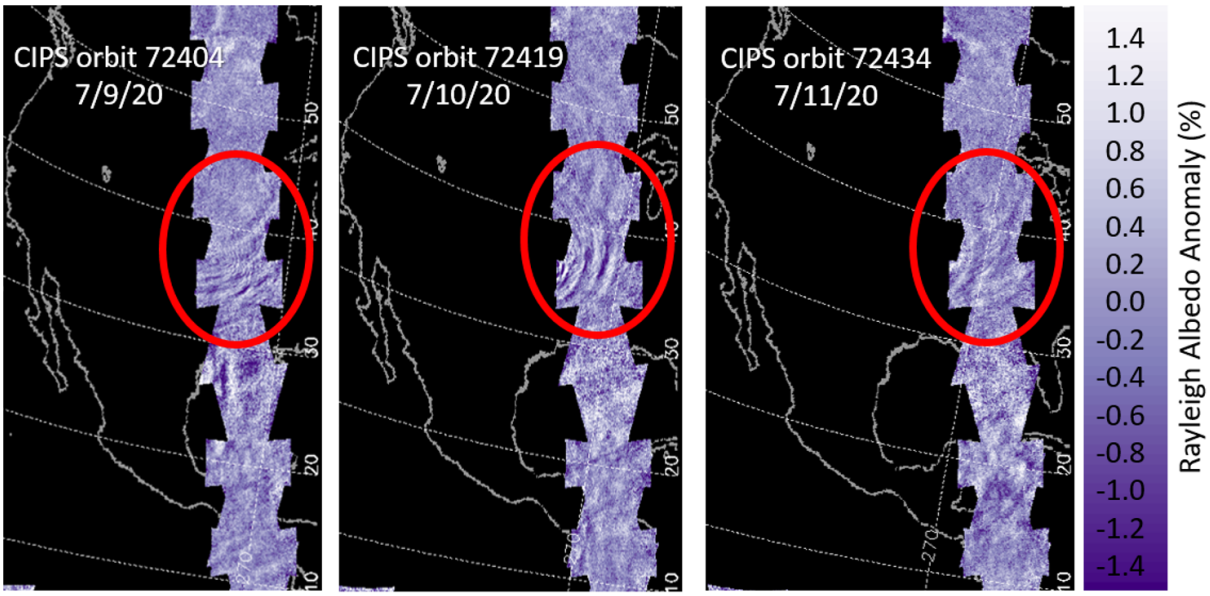

Figure 4. AIM CIPS Rayleigh Albedo Anomaly (version 1.10r05) from the three orbits that passed over the central CONUS on July 9-11, 2020. The individual 4-camera CIPS images inside the highlighted regions were acquired near 15:30 UT each day (ranging from 15:48 UT on July 9 to 15:22 UT on July 11).

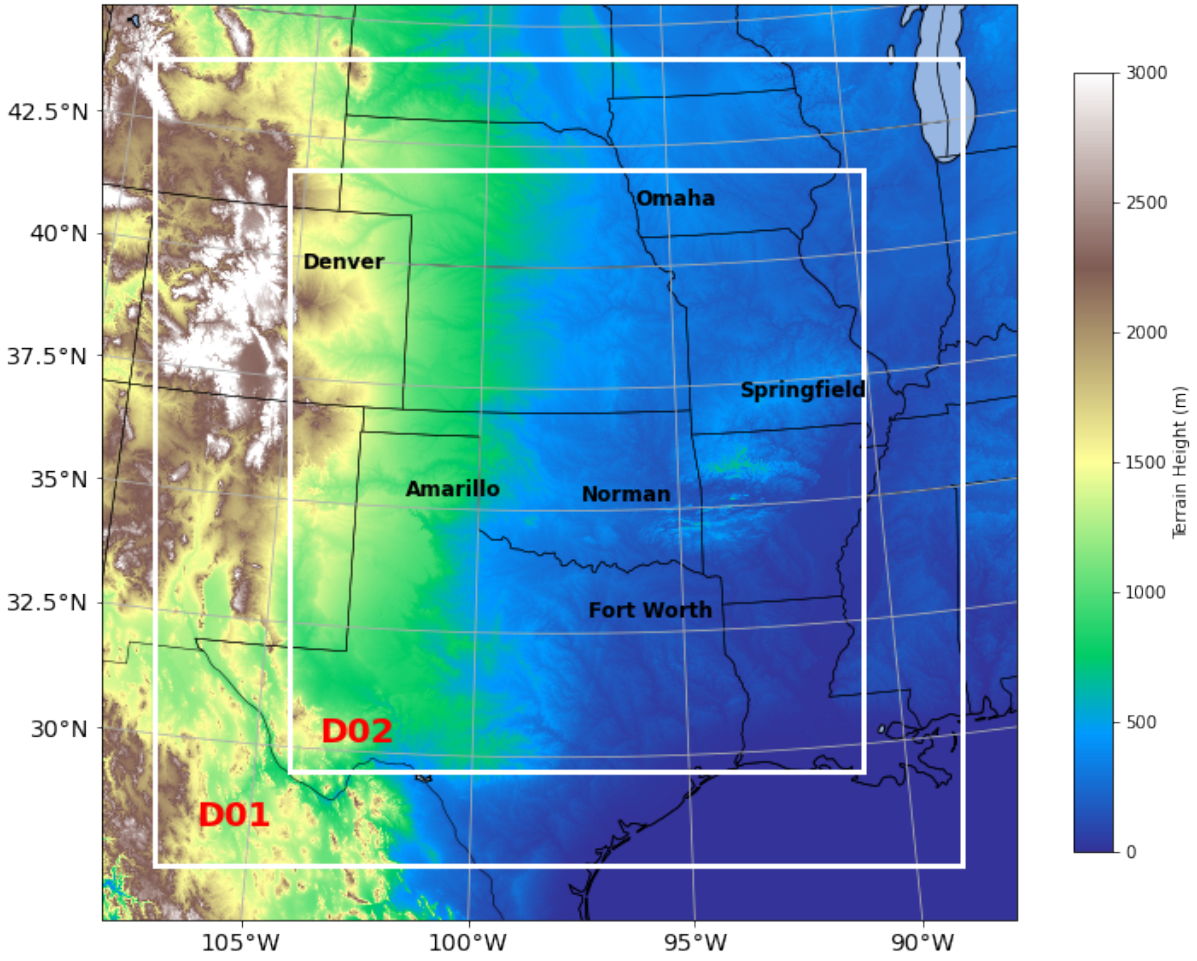

Figure 5. Nested WRF model domains with grid spacing at 6 km (D01) and 2 km (D02) and terrain height (m, color)

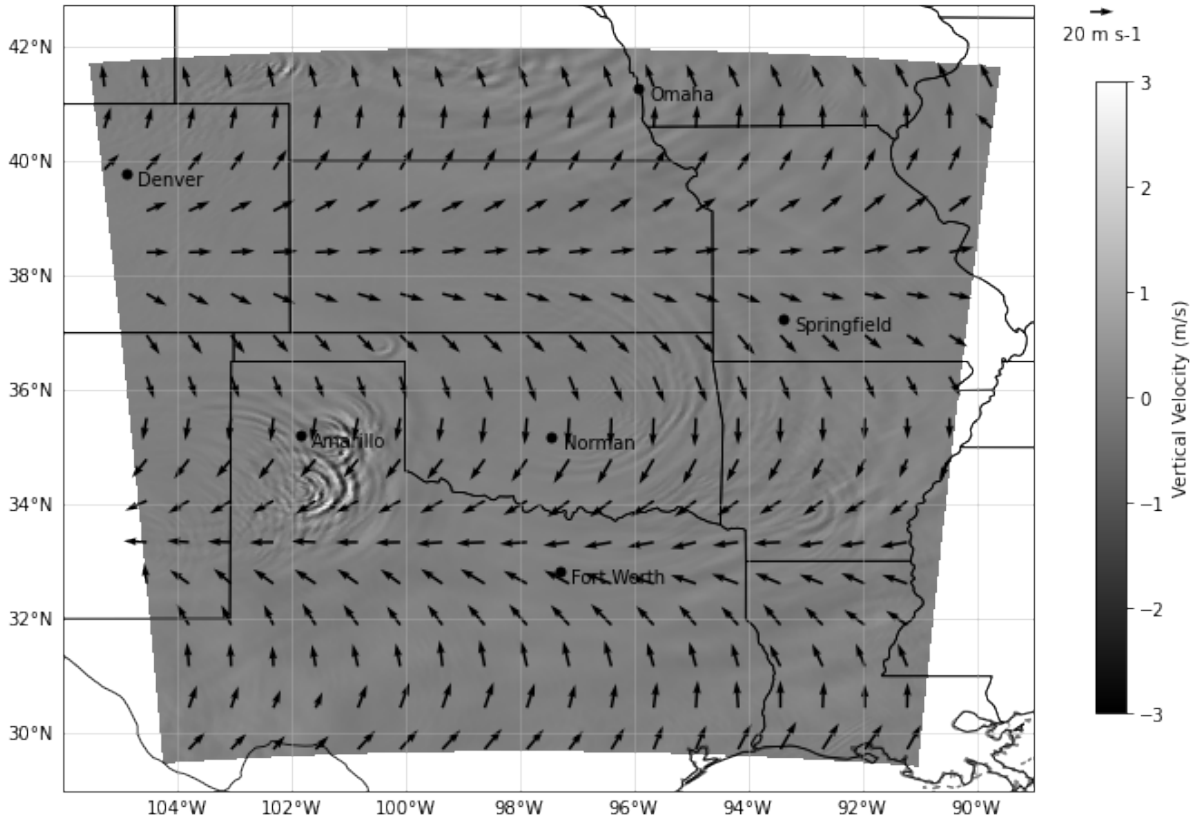

Figure 6. WRF simulated vertical velocity (m/s, gray-scale) and horizontal wind (m/s vector) at 22:30 UT on July 10, 2020 at 30 km altitude. Partial, concentric AGWs are noticeable in the vertical wind throughout the region in the red circle.

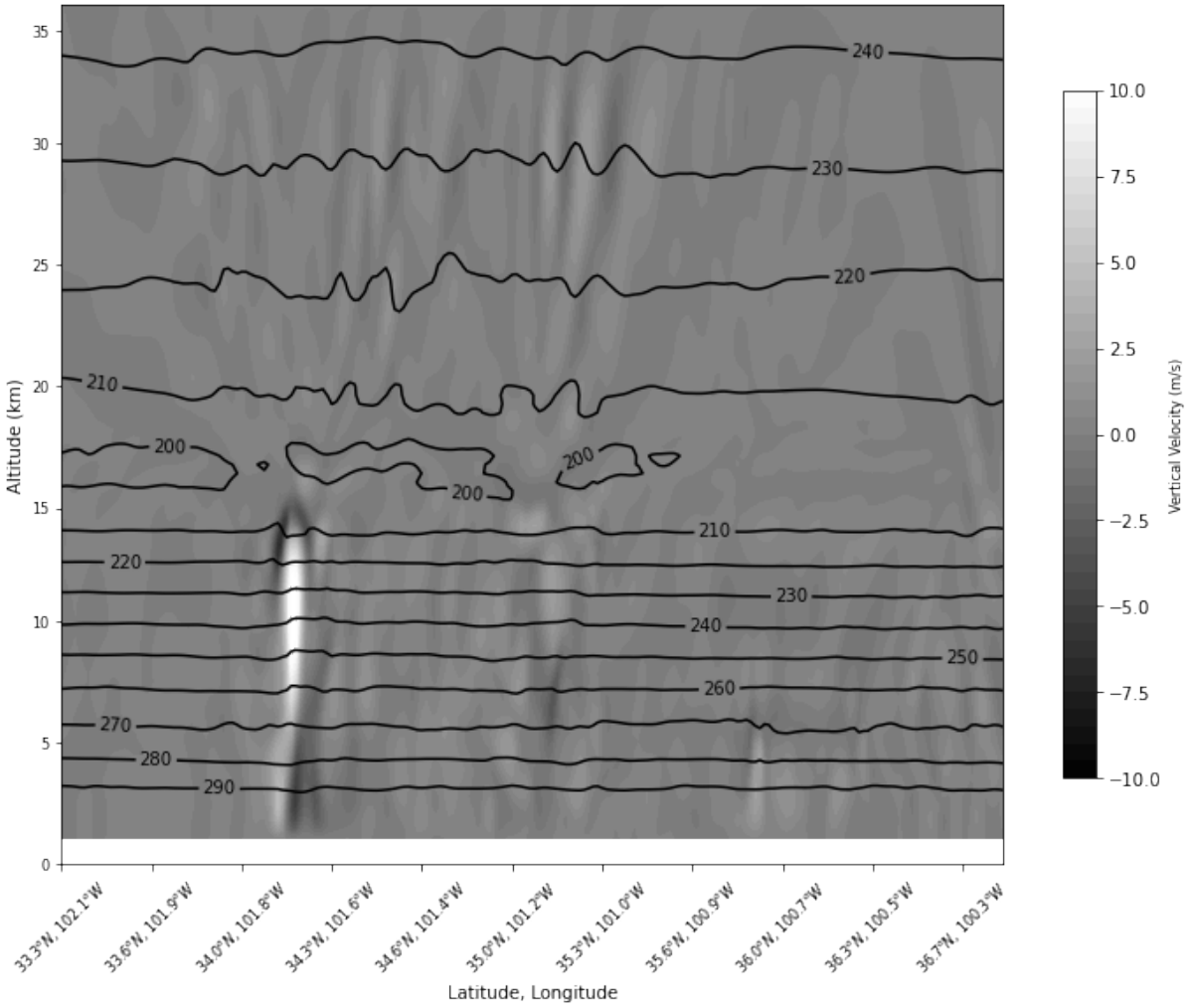

Figure 7. Altitudinal cross-section of WRF vertical wind speed (m/s gray-scale) and air temperature (K, contour lines) through the convective system on July 10, 2020 at 22:30 UT. Negative w indicates downdraft while positive w shows updraft.

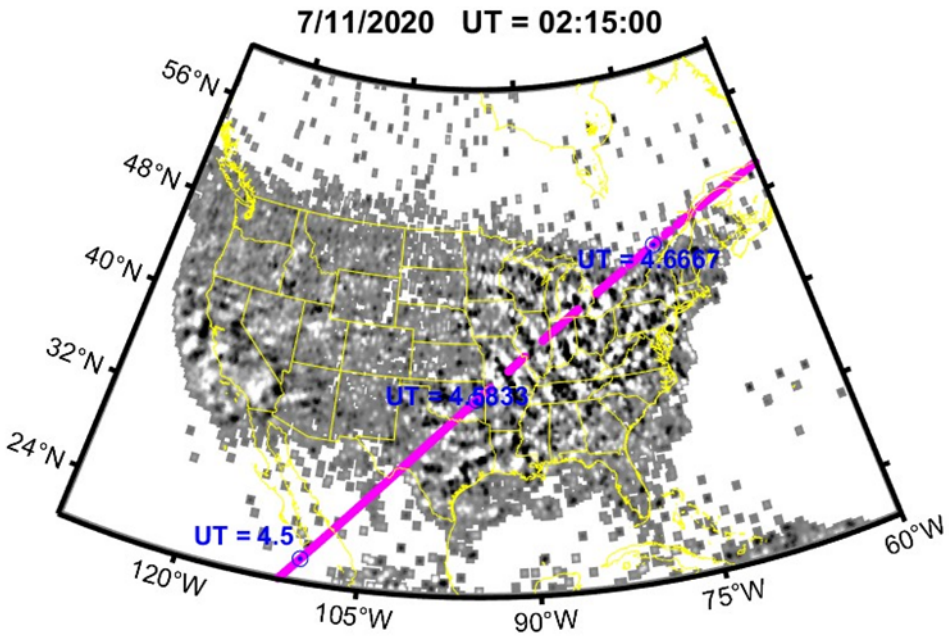

Figure 8. SORTIE IVM measurement track (purple line) overlaid on the near-concentric TIDs seen in GPS TEC data on July 11, 2020 at 2:15 UT. Here, a segment of the SORTIE measurement track from 04:29 to 04:43 UT is shown. The blue text shows the UT times corresponding to the locations of the SORTIE CubeSat denoted by .

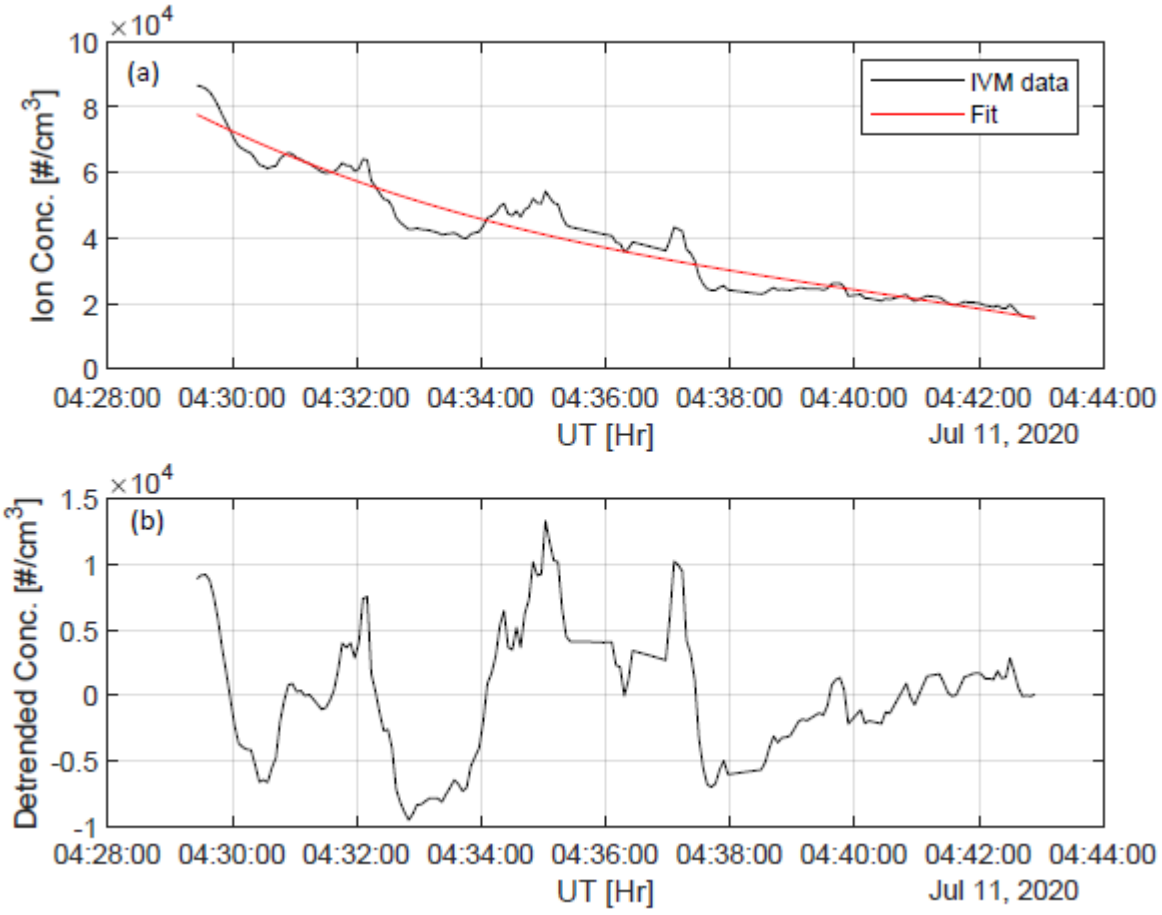

Figure 9. (a) SORTIE 4-s IVM ion density measurements (black line) during the orbit segment shown in Figure 1, and a 3rd-order polynomial fit (red line). (b) Time series of the detrended IVM data calculated by subtracting the fit from the 4-s IVM data.

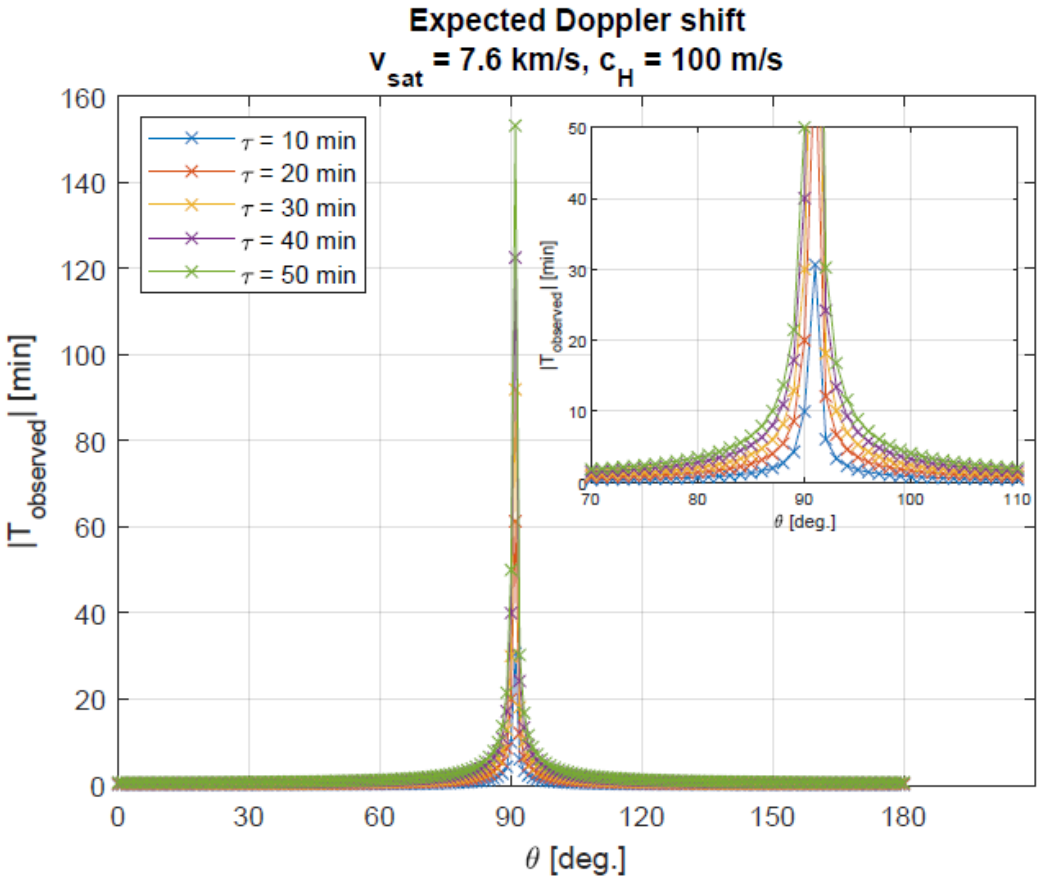

Figure 10. Magnitude of the Doppler-shifted TID periods ($T_{observed}$) in the SORTIE data as a function of the approach angle ( ) relative to the center of concentric rings for different wave periods ( ) with an assumed horizontal phase speed of 100 m/s. The inset figure shows a zoomed view of the Doppler shift between = 70° and 110°. See the text for the definition of approach angle. The inset shows that at = 90°, the observed wave periods are equal to the source periods ( ).

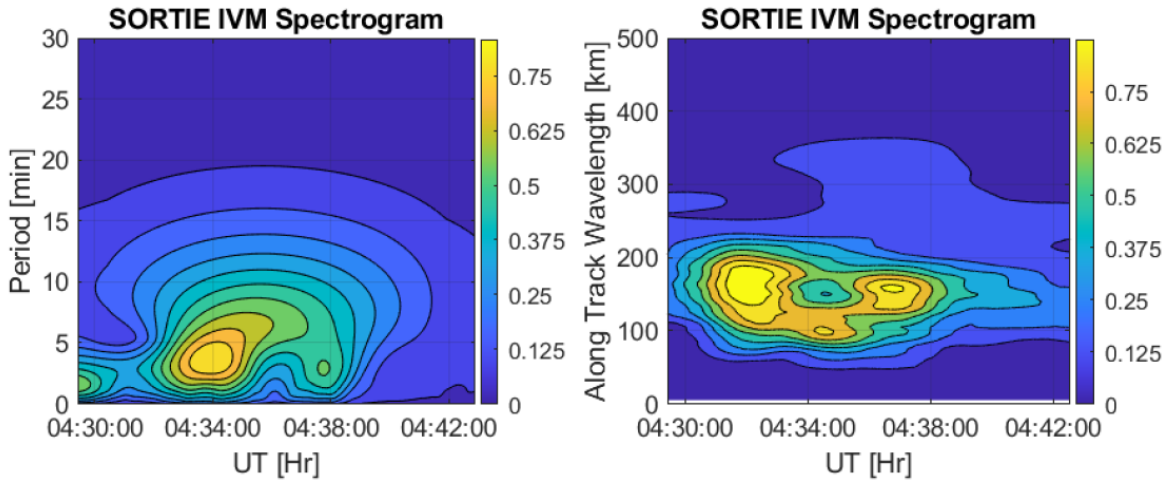

Figure 11. Wavelet spectra of (a) period and (b) along-track wavelength of wave-like perturbation in the SORTIE IVM data as the satellite passed over the near-concentric TIDs seen in the TEC data.